SAND2022-3502J

Processing and Properties of Hf-doped PSZT 95/5 Ceramics

Eric W. Neuman,[1] Nicholas Anselmo,[2] Amber Meyer,[3] Christopher B. Diantonio, Mark A. Rodriguez, Rose Torres, Brian Brane, James G. Griego

Sandia National Laboratories, Albuquerque, NM 87185

Abstract

Niobium doped lead-tin-zirconate-titanate ceramics near the PZT 95/5 orthorhombic AFE – rhombohedral FE morphotropic phase boundary (PSZT 13.5/81/5.5 Nb-1.6) were prepared with up to 10 mol.% of hafnium substituted for zirconium. The ceramics were prepared by a traditional solid-state synthesis route and sintered to near full density at 1150°C for 6 hours in sealed alumina crucibles with self-same material as the lead vapor source. All compositions were ~98% dense with no detectable secondary phases by XRD. Grain size was ~3 µm for all compositions, consisting of equiaxed grains, with intergranular porosity. Compositions exhibited remnant polarization values of ~32 µC/cm^2. Depolarization by the hydrostatic pressure induced FE-AFE phase transition occurred at 310 MPa for all compositions, resulting in a total depolarization output of 32.4 µC/cm^2 for the PSZT ceramics. Evaluation of the R3c-R3m and R3m-Pm$\bar{3}$m phase transition temperatures by impedance spectroscopy showed temperatures on heating ranging from 86 to 92°C and 186 to 182°C, respectively, for increasing nominal Hf content. Thermal hysteresis of the phase transitions was also observed in the ceramics, with transition temperature on cooling being 1-4°C lower. The study demonstrates that the PSZT ceramics are relatively insensitive to variations in hafnium content in the range of 0 to 10 mol.%.

This work was presented in part as “Effect of Hafnium Content on Properties of PSZT” at Materials Science and Technology, Portland, OR, 2019.

[1] Corresponding Author: Sandia National Laboratories, Albuquerque, NM 87185. ewneuma@sandia.gov

[2] Present Address: General Electric Corp., Greenville, SC

[3] Present Address: Lincoln Electric Co., Cleveland, OH

1. Introduction

The perovskites lead zirconate ($PbZrO_3$) and lead titanate ($PbTiO_3$) form a continuous series of solid solutions over the entire composition range.[1] The lead-zirconate-titanate (PZT) system contains a ferroelectric to anti-ferroelectric phase boundary on the lead zirconate rich side of the phase diagram, near the Zr/Ti ratio of 95/5.[1-3] PZT based ferroelectrics near the 95/5 morphotropic phase boundary (PZT95/5) have found use in explosively actuated stand-by power supplies.[4, 5] These devices can supply high current or voltage to devices through the pressure induced phase transformation from the FE-rhombohedral phase to the AFE-orthorhombic phase.[1, 6]

Modification of PZT95/5 with niobium (Nb) has been shown to stabilize the FE Phase, promote densification, enhance breakdown strength, and reduce dielectric loss.[3, 7-11] Additionally, Nb^{5+} acts as a donor dopant, reducing the coercive field (a "soft" PZT), improving breakdown strength, and improving aging characteristics.[3] Modification by tin (Sn) has been shown to stabilize the AFE phase, enhance densification, and reduce the strain associated with the R3c-R3m and R3m-$Pm\bar{3}m$ phase transitions.[12-16] PZT95/5 is typically doped with Nb or co-doping the of Sn^{4+} and Nb^{5+} to tailor the electrical properties and pressure-induced FE-AFE phase transition response in these materials.[4, 6, 13, 14, 17]

Hafnium (Hf) is a naturally occurring impurity in zirconium source materials.[18] Typical concentrations of Hf in natural grades of ZrO_2 are approx. 1 %, but can be as high as 4%. Specialized grades of ZrO_2 can contain concentrations as low as 10's of ppm Hf. The effect of Hf concentration on PZT has been seen limited study.[1, 19] This is perhaps due to the initial reporting that PZT and lead-hafnate-titanate (PHT) have similar electrical properties at ambient conditions, with zirconium being much more plentiful than hafnium. When comparing the PZT and PHT binary phase diagrams (Figure 1), the FE-AFE phase boundary is shifted and does not have the same temperature response. As the

pressure induced FE-AFE phase transition is of interest for explosively actuated power supplies, exploring the effect of Hf on the PZT 95/5 systems is of interest.

This manuscript explores the effect of Hf concentration on the processing, thermal, electrical, and mechano-electrical properties of a niobium doped lead-tin-zirconate-titanate (PSZT) based ceramic.

2. Experimental Procedure

2.1. Processing

This study used commercially available powders (Table I). PSZT ceramics with a composition of $Pb_{0.992}((Zr_{1-x}Hf_x)_{0.81}Ti_{0.055}Sn_{0.135})_{0.9835}Nb_{0.0165}Al_{0.0005}O_3$, with x = 0.00, 0.025, 0.050, 0.075, and 0.10 were fabricated for this study (H0 through H10). The ZrO_2 was pre-milled by ball milling in 4 L baffled HDPE milling jars, in 2-propanol (ACS Grade, Fisher Scientific), using 5 mm diameter YSZ grinding media, at ~90 RPM for 48 h. The ZrO_2 was then pan dried and sieved to -60 mesh (RS 200 Control, Retsch, Haan Germany). All compositions were prepared at a 1 kg nominal batch size. Aluminum nitrate was dissolved in 2-propanol, the batched powders (ZrO_2, PbO, SnO_2, etc.) added, then mixed by ball milling in 1 L baffled HDPE jars, in 2-propanol, using 5 mm diameter YSZ grinding media, at ~90 RPM for 4 h. The slurry was then pan dried and sieved to -20 mesh. The powder was then placed in covered high-purity alumina crucibles (AD998, CoorsTek, Golden, CO) and calcined at 800°C for 4 h in convective air (Thermolyne F48028-80, Thermo Fisher Scientific, Waltham, MA). The calcined powder was ground using a YSZ auto mortar and pestle (RM 200, Retsch), followed by ball milling as previously described. After milling for 4 h, the slurry was pan dried, then sieved to -20 mesh. The powder was then calcined in covered high-purity alumina crucibles at 800°C for 4 h in convective air. The calcined powder was ground using a YSZ auto mortar and pestle, followed by ball milling in 2-propanol. After 4 h, a binder solution was added and mixed by ball milling for an additional 30 min. The binder was 1 wt.% PEG300, 2.5 wt.% PMMA (Dispex CX 4204, BASF Corp. Florham Park, NJ), 0.5 wt.% PEG6000, and 0.5 wt.% oleic

acid. In this binder system, PMMA and PEG6000 acted as the binder, PEG300 as a plasticizer, and oleic acid as a lubricant. The PSZT-organics slurry was dried by automated rotary evaporation, (R-215, Buchi, Flawil, Switzerland) using the 2-propanol setting, at 60 rpm. The dried powder was granulated by lightly grinding with a high-purity alumina mortar and pestle and sieving to -40 mesh. The granulated powder was pressed into approx. 1 in x 1 in x 0.5 in rectangular prisms in polished steel dies at 4 kpsig. The green preforms were then vacuum bagged and cold isostatically pressed (CP92466, Avure Technologies, Västerås, Sweden) to 30 kpsig for 2 min. The green compacts were then heat treated under flowing air to thermally decompose the binder and presinter the compacts (bisque). The bisque parts were then sintered in seasoned high-purity alumina crucibles in a sealed triple crucible configuration (Figure 2). PZT powder with the same composition as the parts was used as the PbO vapor source during sintering, and PZT spacers with the same composition as the parts were used to separate the billets from the crucible. The parts were sintered in a SiC element bottom loading furnace (DT-25-SBL-AE-1088, Deltech Furnaces, Golden, CO) in stagnant air by heating at 1°C/min to 1150°C, isothermally dwelling at 1150°C or 1250°C for 6 h, cooling at 0.5°C/min to 250°C, isothermally dwelling for 2 h, finally cooling to room temperature at 0.2°C/min.

2.2. Characterization

Bulk density of the sintered parts was measured in accordance with ASTM C830, using water as the immersion media and saturation time under vacuum reduced to 5 min. Samples were prepared for X-ray diffraction (XRD) by machining into 10 mm x 10 mm x 1 mm coupons. The coupons were annealed at 400 °C for 1 h in air, with a heating and cooling rate of 1 °C/min. XRD (D2 Phaser, Bruker, Madison, WI) was performed using Cu-K_α radiation, 10-80° 2Θ, 0.02° step, 16.2 s/step. Structural refinement was conducted with TOPAS v5.

Specimens were prepared for microstructural analysis by cross sectioning the billets parallel to the pressing direction, followed by polishing to 0.25 μm using progressively finer diamond abrasives.

The polished cross-sections were etched in 36% HCl for ~2 min at room temperature to reveal grain boundaries. Imaging was performed using light optical microscopy (LOM; MA100N, Nikon Metrology Inc, Brighton, MI), under Köhler illumination with polarized white light. The images were segmented using digital image analysis software (MIPAR v3.4, MIPAR Software, Worthington, OH), and the grain size, equivalent area diameter (EAD), was measured.

Electrical test specimens of 7 mm x 7 mm x 3 mm were machined from the sintered billets. Gold electrodes were sputter-coated on the 7 mm x 7 mm faces and the edges chamfered. Specimens were poled at room temperature by applying an electric field of ± 30 kV/cm at 0.04 Hz in Flourinert FC-33 at room temperature. After poling, the specimens were immediately looped again to generate the P-E hysteresis loop. From the P-E curve, the positive bias coercive field (E_C), positive bias saturated polarization (P_S), and initial remnant polarization (P_R) were calculated. The specimens were then depoled under hydrostatic loading conditions. Total depolarization (Q_H) was calculated from the cumulative depolarization vs. hydrostatic pressure (Q-P) curve, and the hydrostatic depoling pressure (P_H, pressure at which FE to AFE transformation is induced) was calculated from the peak in the 1st derivative of the Q-P curve.

Dielectric spectroscopy (HP4294A, Agilent Technologies, Santa Clara, CA) was performed as a function of temperature (EC1A, Sun Electronic Systems, Inc., Titusville, FL) on the unpoled specimens. Specimens were heated at a rate of 2°C per min to 250°C then cooled to room temperature at 2 °C/min. The R3c ↔ R3m and R3m ↔ $Pm\bar{3}m$ phase transformation temperatures were calculated from the peak in the Tan δ vs. T curve and the κ vs. T curve, at a frequency of 1 kHz, respectively. Data analysis was performed using DIAdem 2019 (National Instruments, Austin, TX), JMP 14.2 (SAS Institute Inc, Cary, NC), and OriginPro 2020b (Origin Labs, Northampton, MA).

3. Results and Discussion

The sintered bulk densities are summarized in Table II. After sintering, parts exhibited thermal stress cracks extending approx. 1-2 mm into the billets (not shown). Density increased steadily with increasing Hf concentration, from 8.00 to 8.18 g/cm^3 for 0 to 10 mol% Hf substitution, respectively, for the material sintered at 1150°C (Figure 3). Similarly, for the ceramics sintered at 1250°C, density increased from 7.97 to 8.16 g/cm^3 for 0 to 10 mol% Hf substitution. Increasing the sintering temperature from 1150 to 1250°C resulted in a decrease in density of approx. 0.02 g/cm^3 for all compositions. XRD identified the compositions as all having the R3c structure, with no additional phases (i.e., ZrO_2, PbO, the Pbam structure, etc.) detected by XRD (Figure 4). Lattice parameters were calculated by Rietveld refinement (Table III). The a- and c-axis parameters both decreased with increasing Hf concentration (Figure 5). The a-axis decreased from 5.835 to 5.834 Å, and the c-axis decreased from 14.373 to 14.366 Å from 0 to 10 mol.% Hf substitution, respectively. These minute changes in lattice parameters are consistent with the differences in ionic radii for Zr^{4+} and Hf^{4+} with 6-fold coordination of 0.72 and 0.71 Å, respectively. Crystallographic density was calculated using the measured lattice parameters and nominal stoichiometry for each composition, shown in Table II. From the calculated crystallographic densities, all compositions were approx. 98% dense.

Representative polished and chemically etched microstructures of the sintered Hf-doped PSZT ceramics are shown in Figure 6. Grain size, EAD and the DeBrouckere mean diameter (D[4,3]), and distribution statistics are summarized in Table IV. The material exhibited a finer grain size near the surface of the billets, approx. 1-3 mm thick, and a larger grain size in the core of the billet. Reported grain sizes were taken from the core region of the sintered billets. Grain size was approx. 3.1 ± 1.5 µm, unchanging with increasing Hf content (P = 0.7834; Figure 7). The D[4,3], was ~ 5.8 µm for Hf substitution between 0 and 5 mol.%, decreasing to 4.5 and 5.0 µm for 7.5 and 10 mol.% Hf substitution, respectively. Conversion to the volume weighted distribution shows similar grain sizes for the

compositions. The Dv10 was ~ 3 μm for all compositions. The Dv50 value, volume weighted median, was approx. ~5.1 μm for 0 to 5 mol.% and ~4.5 μm for 7.5 to 10 mol.% Hf substitution. The 0 to 5 mol.% Hf substituted compositions had a Dv90 of ~ 5.8 μm, decreased to ~4.7 μm for 7.5 and 10 mol.% Hf substitution. Porosity was predominantly intergranular and uniformly distributed. Thus, grain size of the PSZT ceramics appears to be relatively unchanging with changes in Hf content.

Polarization and coercive field, for the samples sintered at 1150°C for 6 h, were measured by P-E hysteresis looping (Figure 8). Saturated polarization, remnant polarization, and coercive field values are summarized in Table V. Saturated polarization decreased slightly from 36.1 to 35.4 μC/cm^2 (Figure 9) as the amount of Hf substitution increased from 0 to 10 mol.% but was not statistically significant (P = 0.2243). Remnant polarization slightly decreased as Hf substitution increased from 0 to 10 mol.% (Figure 9), from 32.1 to 31.4 μC/cm^2, respectively, and was not statistically significant (P = 0.1938). Thus, charge storage decreases with increasing Hf substitution since polarization remains unchanged, but density increases. The coercive field decreased from 9.31 ± 0.07 kV/cm for the sample without Hf addition, to 9.09 ± 0.05 kV/cm for the sample where 10 mol.% Hf was substituted for Zr, Figure 9. This was a 2.4% decrease, and was statistically significant, having P-value of 0.0029. The initial poling field is ~1.6 kV/cm higher than the coercive field for H0, decreasing to ~0.6 kV/cm for H10. The mechanism by which the Hf substitution lowers the initial poling field and coercive field is not understood. As Zr and Hf have the same ionic radii, electron structure, coordination, and valence, the change in coercive field with Hf substitution is unexpected. Thus, substitution of Hf for Zr up to 10 mol.% resulted in no change to the polarization values of the samples and a small decrease in coercive field value.

Room temperature pressure induced depolarization via the FE to AFE phase transition was measured for the samples sintered at 1150°C for 6 h (Figure 10). As pressure is increased, a small amount of charge is released, due to the direct piezoelectric effect, until reaching ~300 MPa, at which the R3c phase converts to the Pbam phase, releasing all stored space charge. Further increasing

pressure does not result in the release of any additional charge. The samples tested all exhibited a sharp transition, with relatively little curvature before and after the transition, indicating chemical homogeneity within the samples. Table VI summarizes the calculated depolarization pressure and maximum total depolarization for the PSHZT ceramics. Depolarization occurred at approx. 310 MPa regardless of Hf content (P = 0.3493), shown by Figure 11. Similarly, total depolarization of was approx. 32.4 $\mu C/cm^2$ for all compositions (P = 0.7847). Thus, substitution of up to 10 mol.% Zr for Hf did not affect the room temperature hydrostatic depoling characteristics of the PSHZT ceramics.

Phase transition temperatures were measured for the Hf-doped PSZT ceramics sintered at 1150°C for 6 h (Figure 12). The calculated phase transition temperatures on heating and cooling are summarized in Table VII. On heating, the R3c-R3m phase transition temperature increased from 86 to 92°C (P = 0.0142) and the R3m to $Pm\bar{3}m$ transition temperature decreased from 186 to 182°C (P = 0.0089) as Hf substitution increased from 0 to 10 mol.%, respectively (Figure 13). Upon cooling, the $Pm\bar{3}m$ to R3m transition temperature decreased from 185 to 179°C (P = <0.0001) as increasing Hf was substituted for Zr from 0 to 10 mol.% and the R3m to R3c phase transition temperature increased from 83 to 88°C (P = 0.0021) for the same increase in Hf content. The material exhibits thermal hysteresis, with the R3c to R3m transition occurring approx. 3°C higher on heating than on cooling, and the R3m to $Pm\bar{3}m$ phase transition occurring approx. 2°C higher on heating than cooling. This thermal hysteresis behavior is the result of these being 1st order transitions and has been previously reported.[3, 20] Increasing Hf content resulted in an ~6.5% increase in the R3c to R3m transition temperature and an ~2.5% increase in the R3m to $Pm\bar{3}m$ transition temperature.

These results demonstrate that the presence of Hf in niobium doped lead-tin-zirconate titanate has negligible effects on processing and properties of these ceramics. While bulk density increases with increasing Hf content, relative density, grain size, polarization, depolarization pressure, and depolarization output remain relatively unchanged. Small but significant changes in coercive field, and

R3c-R3m and R3m-Pm$\bar{3}$m phase transition temperatures are observed. The study investigated a range of Hf concentration five times the typical ~1% and two and a half times the maximum ~4% concentration for naturally occurring Hf impurity in zirconium sources. Thus, there is little expectation that a practical difference in properties exists between the use low-Hf and natural purity grades of zirconium source materials in PSZT.

4. Summary

Niobium doped lead-tin-zirconate-titanate ceramics near the PZT 95/5 morphotropic phase boundary were prepared with up to 10 mol.% of hafnium substituted for zirconium. The ceramics were prepared by a traditional solid-state synthesis route and sintered to near full density at 1150°C for 6 hours in sealed alumina crucibles with self-same material as the lead vapor source. The sintered ceramics exhibited the following properties:

- Sintered density increased from 8.00 to 8.16 g/cc as Hf substitution increased from 0 to 10 mol.% and all compositions were ~98% dense with no detectable secondary phases.
- Grain size was 3 μm for all compositions, consisting of equiaxed grains, with intergranular porosity.
- Saturated polarization values of 36 μC/cm^2, remnant polarization values of 32 μC/cm^2, and coercive field values of between 9.1 and 9.3 kV/cm, increasing with Hf content.
- Depolarization by the pressure induced FE-AFE phase transition occurred at 310 MPa for all compositions, with a total depolarization output of 32.4 μC/cm^2.
- Evaluation of the R3c-R3m and R3m-Pm$\bar{3}$m phase transition temperatures showed temperatures on heating ranging from 86 to 92°C and 186 to 182°C, respectively, for increasing Hf content. Thermal hysteresis was also observed, with transition temperature on cooling being ~3 and ~2°C lower for the R3c-R3m and R3m-Pm$\bar{3}$m, respectively.

The study demonstrates that the PSZT 95/5 ceramics are relatively insensitive to variations in hafnium content in the range of 0 to 10 mol.% Hf substituted for Zr. This outcome is consistent with expectations given the similar ionic radii and valence electron orbital structure of Zr^{4+} and Hf^{4+}. At room temperature, the compositions were insensitive to changes in depolarization pressure and depolarization output with the changes in hafnium content. This demonstrates that manufacturing processes for PSZT for ferroelectric generators can reasonably ignore hafnium content, using natural Hf grade zirconium sources, without impact to pressure induced depolarization behavior. Effect of hafnium content on performance at temperatures other than ambient continue to be unreported and open for future exploration.

Acknowledgements

The authors would like to thank the Active Ceramics Value Stream organization, Analytical Technologies Value Stream organization, The Ferroelectric Neutron Generator, Neutron Tube, and Active Ceramics Lifecycle Engineering organization, and The Material Characterization & Performance department of Sandia National Laboratories for their assistance with sample preparation and characterization. The authors thank Dr. Sean Bishop Dr. Wen Dong and of Sandia National Laboratories for their assistance in reviewing the manuscript.

Sandia National Laboratories is a multi-mission laboratory managed and operated by National Technology and Engineering Solutions of Sandia, LLC, a wholly owned subsidiary of Honeywell International Inc., for the U.S. Department of Energy's National Nuclear Security Administration under contract DE-NA0003525. This paper describes objective technical results and analysis. Any subjective views or opinions that might be expressed in the paper do not necessarily represent the views of the U.S. Department of Energy or the United States Government.

Author Contribution Statement

E. Neuman designed the study, analyzed the data, and supervised the project. N. Anselmo, A Meyer, R. Torres, and B. Brane performed the experiments. M. Rodriguez and J. Griego performed XRD measurement and analysis. E. Neuman wrote the manuscript with input from C. Diantonio and M. Rodriguez.

References

1. Jaffe B, Cook WR, Jaffe H. Piezoelectric Ceramics. New York, NY: Academic Pricess Inc.; 1971.
2. Dai X, Xu Z, Viehland D. Effect of Oxygen Octahedron Rotations on the Phase Stability, Transformational Characteristics, and Polarization Behavior in the Lead Zirconate Titanate Crystalline Solution Series. Journal of the American Ceramic Society. 1995;78(10):2815-27.
3. Berlincourt D, Krueger HHA, Jaffe B. Stability of phases in modified lead zirconate with variation in pressure, electric field, temperature and composition. Journal of Physics and Chemistry of Solids. 1964;25(7):659-74.
4. Lysne PC, Percival CM. Electric energy generation by shock compression of ferroelectric ceramics: Normal−mode response of PZT 95/5. Journal of Applied Physics. 1975;46(4):1519-25.
5. Setchell RE. Shock wave compression of the ferroelectric ceramic Pb0.99(Zr0.95Ti0.05)0.98Nb0.02O3: Depoling currents. Journal of Applied Physics. 2005;97(1):013507.
6. Fritz IJ, Keck JD. Pressure-temperature phase diagrams for several modified lead zirconate ceramics. Journal of Physics and Chemistry of Solids. 1978;39(11):1163-7.
7. Yang P, Voight JA, Lockwood SJ, Rodriguez MA, Burns GR, Watson CS. The Effect of Lead Stoichiometry on the Dielectric Performance of Niobium Modified PZT 95/5 Ceramics. In: Nair KM, Bhalla AS, Hirano S-I, Suvorov D, Zhu W, Schwartz R, editors. Ceramic Materials and Multilayer Electronic Devices. Ceramics Transactions. 150. Weterville, OH: The American Ceramic Society; 2004. p. 289-98.
8. Yang P, Voigt JA, Rodriguez MA, Moore RH, Bums GR. Effects of Niobium Addition on Microstructural and Electrical Properties of Lead Zirconate Titanate Solid Solution (PZT 95/5). Advances in Electronic Ceramic Materials: Ceramic Engineering and Science Proceedings2005. p. 187-95.

9. Noheda B, Gonzalo JA, Hagen M. Pulsed neutron diffraction study of Zr-rich PZT. Journal of Physics: Condensed Matter. 1999;11(20):3959-65.

10. García C, Aragó C, Gonzalo JA. Composition and Field Dependence of the Thermal Hysteresis at the F RL -F RH Phase Transition in Zr-Rich PbZr 1−x Ti x O 3. Ferroelectrics. 2002;272(1):381-6.

11. Kojima S, Ohta N, Dong X. Stability of Antiferroelectric and Ferroelectric Phases in Low Ti Concentration PbZr1-xTixO3. Japanese Journal of Applied Physics. 1999;38(Part 1, No. 9B):5674-8.

12. Berlincourt D, Jaffe H, Krueger H, Jaffe B. Release of electric energy in PbNb (Zr, Ti, Sn) O3 by temperature-and by pressure-enforced phase transitions. Applied Physics Letters. 1963;3(5):90-2.

13. Berlincourt DA, Krueger HHA. Research on Piezoelectric Materials and Phenomena: Annual Progress Report, February 1, 1961 through January 31, 1962; Sandia Corporation Purchase Order No. 51-9689. Cleveland Ohio: Clevite Corporation, Division ER; 1962. Contract No.: Project No. 30202.

14. Berlincourt DA, Krueger HHA. Research on Piezoelectric Materials and Phenomena: Annual Progress Report, February 1, 1962 through December 31, 1962; Sandia Corporation Purchase Order No. 51-9689A. Cleveland Ohio: Clevite Corporation, Division ER; 1963. Contract No.: Project No. 323110.

15. DiAntonio CB, Rae DF, Corelis DJ, Yang P, Burns GR. Thermal properties of PZT95/5 (1.8 Nb) and PSZT ceramics. Sandia National Laboratories; 2006. Report No.: SAND2006-5437.

16. Zhiming C, Jingyu L, Yongling W. Phase transition studies of PSZT ceramics with vertical ferro-antiferroelectric phase boundary. Ferroelectrics. 1990;101(1):225-34.

17. Shkuratov SI. Explosive Ferroelectric Generators: From Physical Principles to Engineering. Hackensack, NJ: World Scientific Publishing Co. Pte. Ltd.; 2019.

18. Sinton CW. Raw materials for glass and ceramics: sources, processes, and quality control. Hoboken, NJ: John Wiley & Sons, Inc.; 2006.

19. Hall CA, Dungan RH, Stark AH. Solid Solutions in Antiferroelectric Region of the System PbHfO3-PbTiO3-PbSnO3-PbNO2O6. Journal of the American Ceramic Society. 1964;47(6):259-64.

20. Yang P, Payne DA. Thermal stability of field-forced and field-assisted antiferroelectric-ferroelectric phase transformations in Pb(Zr,Sn,Ti)O3. Journal of Applied Physics. 1992;71(3):1361-7.

List of Figures

Tables

Table I. Summary of raw materials used. Particle size is the D50 reported from the supplier CoA.

Material	Vendor	Grade	Purity	Particle Size (µm)
PbO	Hammond	100Y	99.95%	< 6
ZrO_2	Materion	Z-1042	99.7% 80 ppm Hf	6.03 0.53†
SnO_2	Materion	T-1137	99.9%	0.23
TiO_2	Materion	T-1156	99.9%	0.52
Nb_2O_5	H.C. Starck	Ceramics Grade	99.9%	0.6
HfO_2	Materion	H-1101	99.95 547 ppm Zr	0.31
$Al(NO_3)_3 \cdot 9H_2O$	Sigma-Aldrich	ACS	≥ 98%	--
PEG300	BASF	Kollisolv 300	--	--
PEG6000	Alfa-Aesar	A17541	--	--
PMMA	BASF	Dispex CX 4204	--	--
Oleic Acid	Sigma-Aldrich	Technical	> 95%	--

†measured after pre-milling

Table II. Summary of density and open porosity for the sintered PSHZT ceramics.

ID	Sintering Temperature (°C)	Sintered Bulk Density (g/cm³)	Relative Density (%)	N
H0	1150	8.003 ± 0.006	98.0	6
	1250	7.974 ± 0.008	--	4
H2.5	1150	8.016 ± 0.014	97.7	5
	1250	8.016 ± 0.010	--	4
H5	1150	8.080 ± 0.016	97.9	6
	1250	8.059 ± 0.007	--	4
H7.5	1150	8.131 ± 0.008	98.0	5
	1250	8.108 ± 0.013	--	4
H10	1150	8.179 ± 0.007	98.1	5
	1250	8.155 ± 0.008	--	4

Table III. Summary of calculated R3c lattice parameters and crystallographic density from structure refinement of the XRD patterns for the PSHZT ceramics.

ID	a-axis (Å)	c-axis (Å)	Crystallographic Density (g/cm^3)
H0	5.8356 ± 0.0001	14.3730 ± 0.0003	8.164
H2.5	5.8354 ± 0.0001	14.3714 ± 0.0004	8.206
H5	5.8350 ± 0.0001	14.3701 ± 0.0003	8.249
H7.5	5.8337 ± 0.0001	14.3659 ± 0.0003	8.296
H10	5.8337 ± 0.0001	14.3669 ± 0.0003	8.337

Table IV. Summary of the equivalent area diameter for the PSHZT ceramics sintered at 1150 °C for 6 h.

	Grain Size (µm)					
ID	EAD	Dv10	Dv50	Dv90	D[4,3]	N
H0	3.12 ± 1.51	3.00	5.05	8.97	5.72	2356
H2.5	3.09 ± 1.52	2.93	5.27	9.59	5.81	2625
H5	3.22 ± 1.54	3.04	5.24	9.89	5.91	2489
H7.5	2.87 ± 1.27	2.66	4.32	6.71	4.54	3159
H10	3.30 ± 1.43	3.06	4.88	7.10	5.02	2412

Table V. Summary of saturated polarization, initial remnant polarization, and coercive field for the PSHZT ceramics sintered at 1150°C for 6 h.

Sublot No.	Ps ($\mu C/cm^2$)	Pr ($\mu C/cm^2$)	Ec+ (kV/cm)	N
H0	36.06 ± 0.34	32.13 ± 0.35	9.31 ± 0.07	5
H2.5	36.72 ± 0.54	32.58 ± 0.41	9.21 ± 0.04	4
H5	35.69 ± 0.46	31.68 ± 0.33	9.19 ± 0.05	3
H7.5	36.07 ± 0.28	32.06 ± 0.39	9.13 ± 0.05	5
H10	35.43 ± 0.41	31.41 ± 0.36	9.09 ± 0.05	5

Table VI. Summary of depoling pressure (at 15 μC/cm^2 depolarization) and maximum depolarization for the PSHZT ceramics sintered at 1150°C for 6 h.

ID	Ph (MPa)	Qh (μC/cm^2)	N
H0	313.4 ± 3.6	32.45 ± 0.42	5
H2.5	308.1 ± 2.5	32.52 ± 0.82	5
H5	306.1 ± 3.4	32.21 ± 0.36	4
H7.5	311.7 ± 5.8	32.61 ± 0.12	4
H10	305.8 ± 3.1	32.32 ± 0.37	4

Table VII. Summary of R3c-R3m-Pm$\bar{3}$m phase transition temperature hysteresis for the PSHZT ceramics sintered at 1150°C for 6 h.

ID	Transition Temperature (°C)			
	R3c to R3m	R3m to R3c	R3m to Pm$\bar{3}$m	Pm$\bar{3}$m to R3m
H0	86	83	186	185
H2.5	88	85	185	184
H5	89	86	183	182
H7.5	89	87	183	181
H10	92	88	182	179

Measurement error is ± 1.2°C for all measurements.

Figures

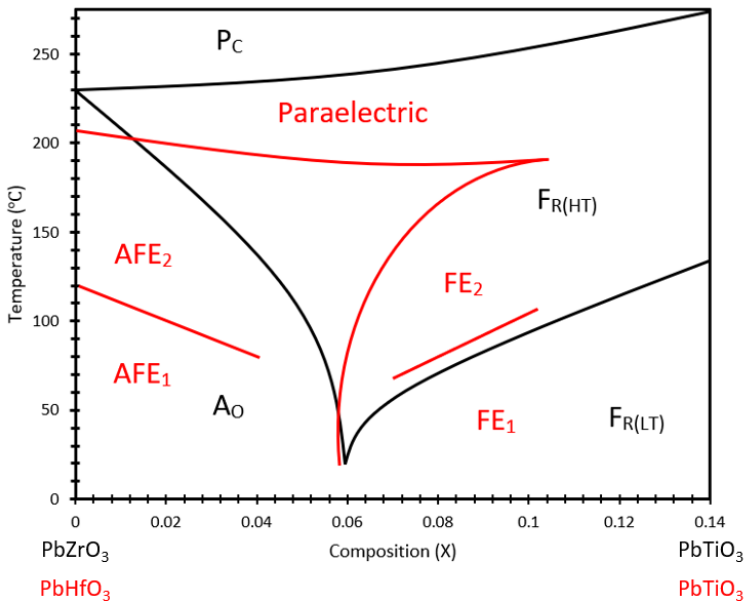

Figure 1. $PbZrO_3$-$PbTiO_3$ and $PbHfO_3$-$PbTiO_3$ binary phase diagrams in the $PbZrO_3$ / $PbHfO_3$ rich region.[1, 19]

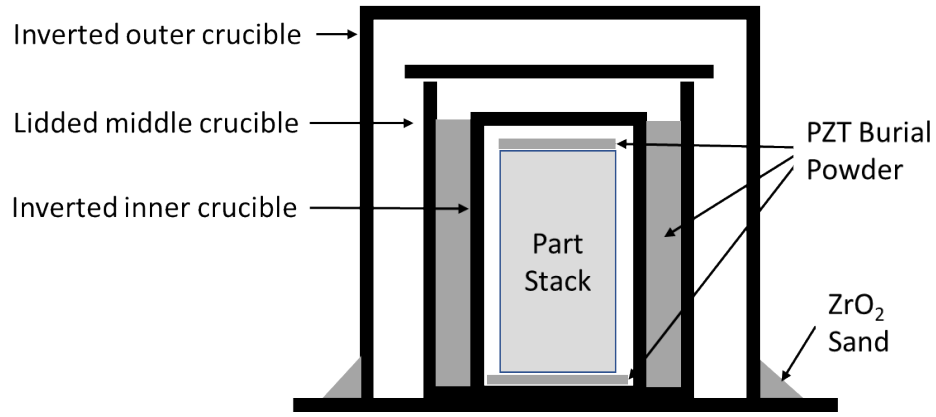

Figure 2. Schematic of the sealed triple crucible configuration used to sinter the PSHZT ceramics.

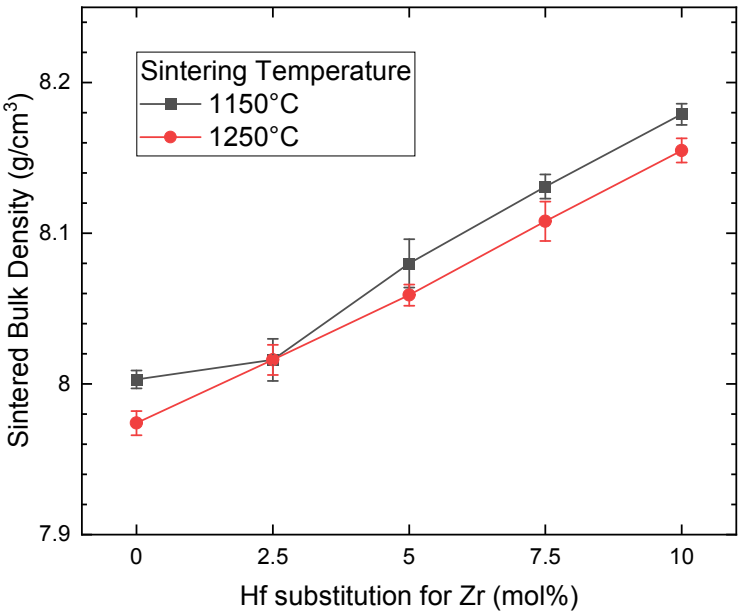

Figure 3. Sintered bulk density as function of Hf substitution in the PSHZT ceramic.

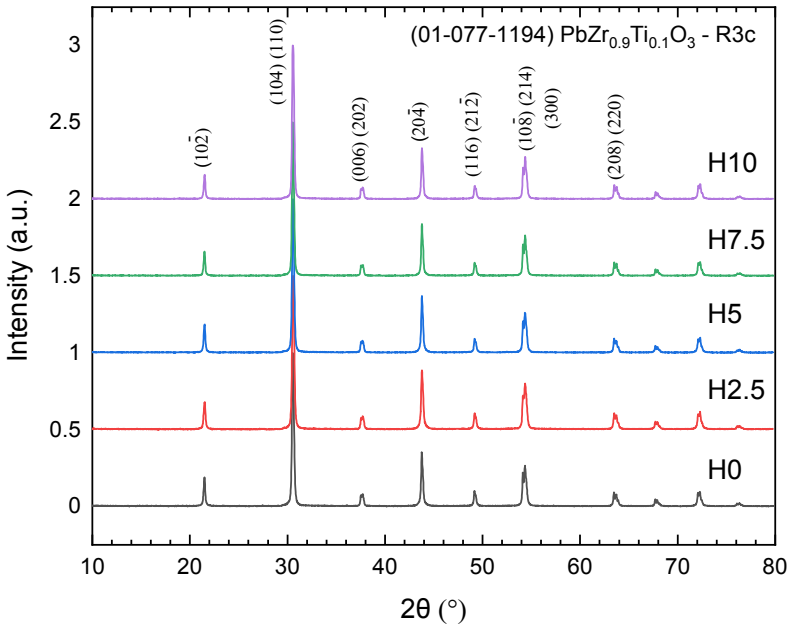

Figure 4. XRD patterns for the PSHZT ceramics.

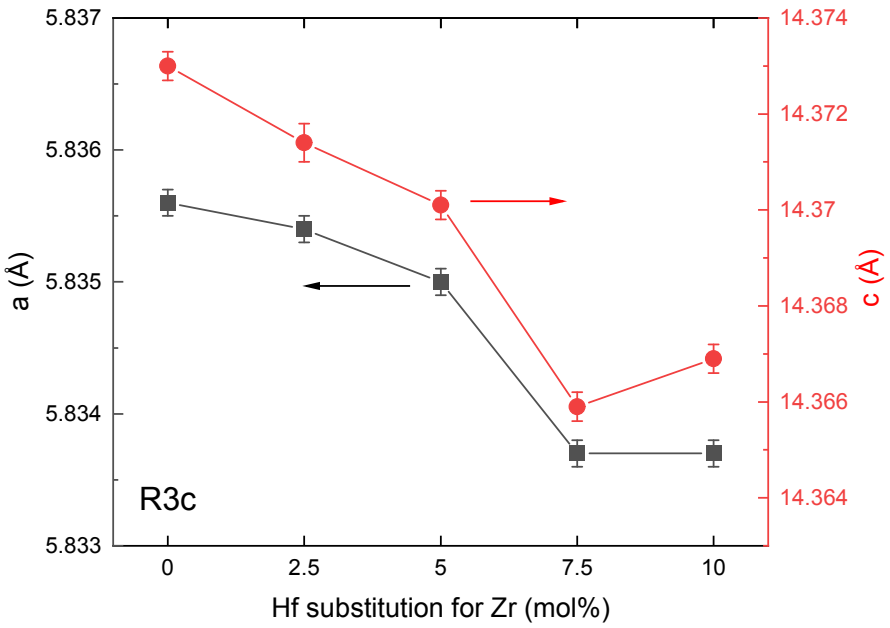

Figure 5. Calculated lattice parameters as a function of Hf substitution for the PSHZT ceramics.

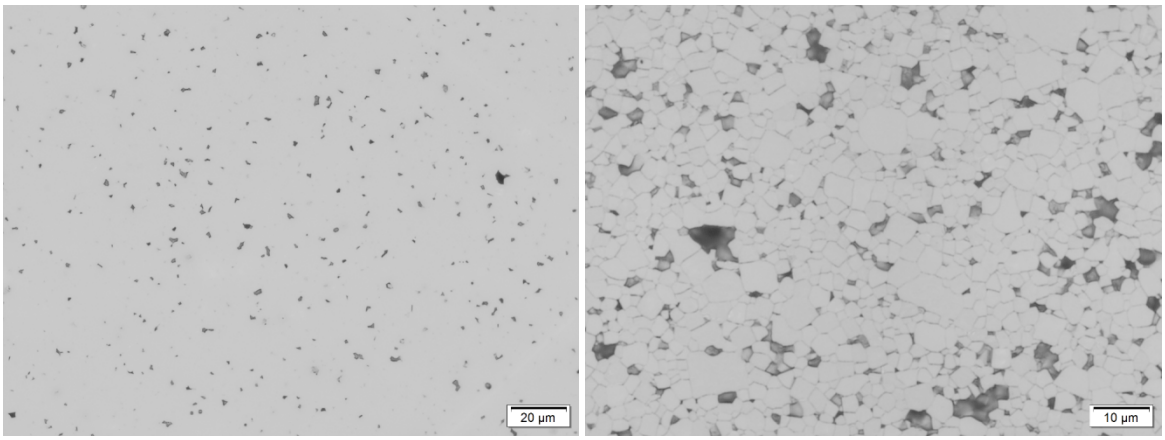

Figure 6. Light optical micrographs of the polished (left) and chemically etched (right) cross-sections of the PSHZT ceramic. H2.5 is shown as representative of all compositions.

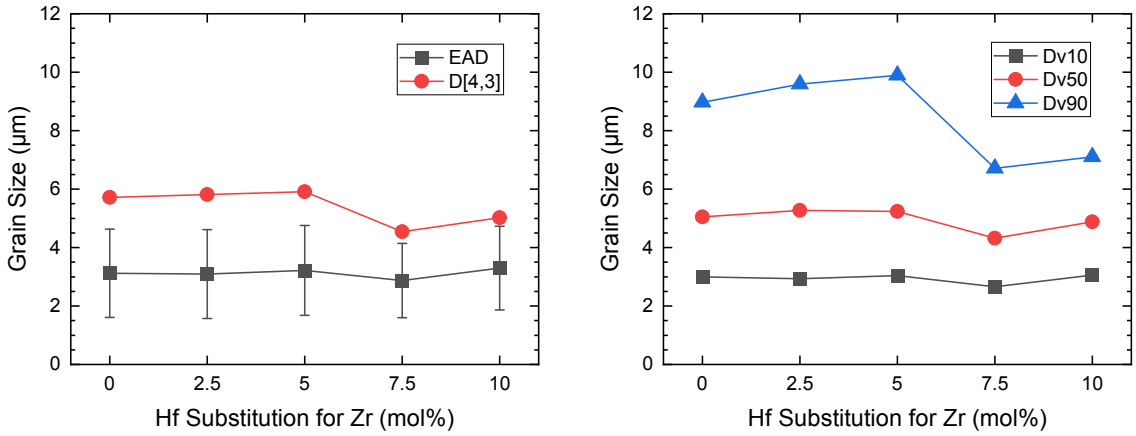

Figure 7. Grain size descriptors as function of Hf substitution in the PSHZT ceramic.

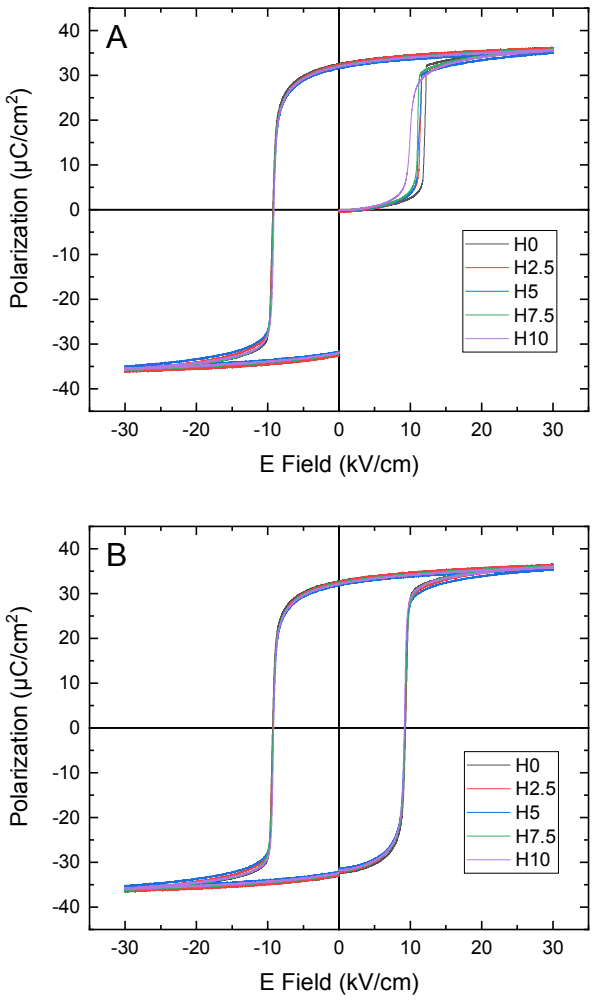

Figure 8. P-E hysteresis loops for the PSHZT ceramics: A) initial poling loop; B) full loop.

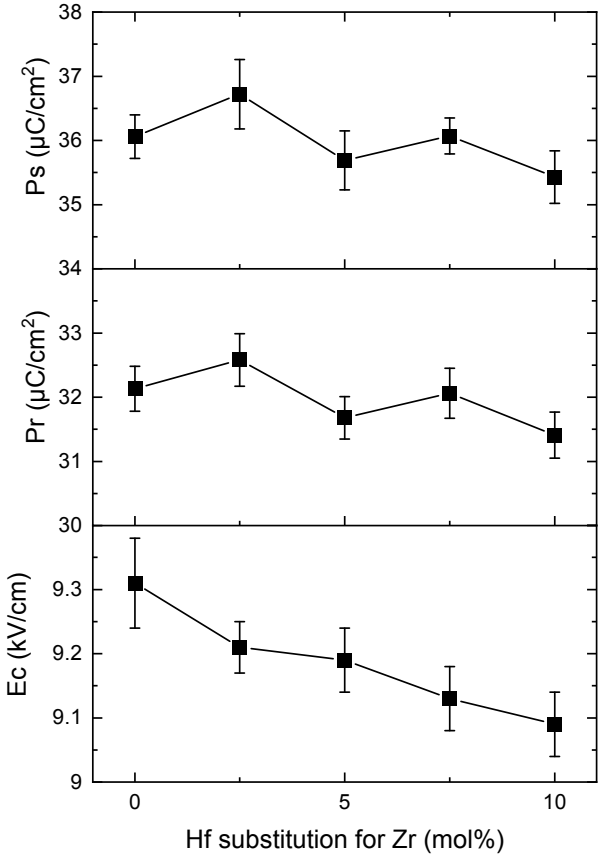

Figure 9. Saturated polarization, remnant polarization, and coercive field as function of Hf substitution in the PSHZT ceramic.

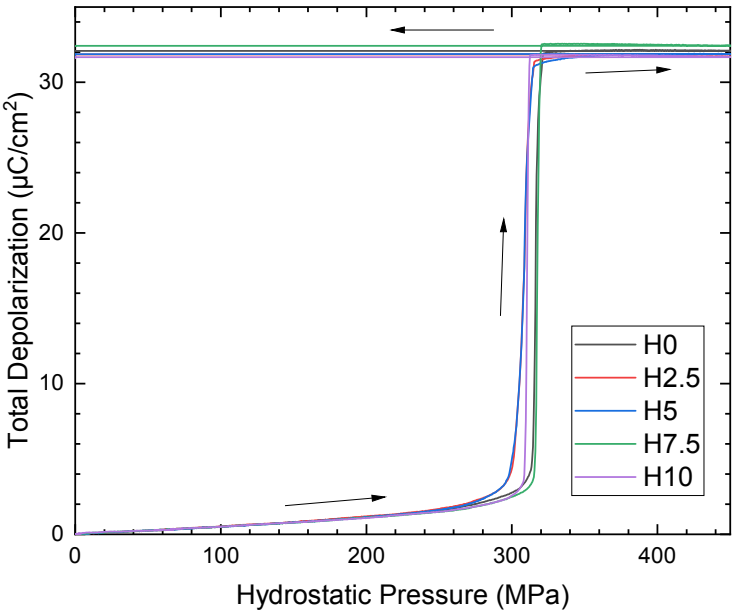

Figure 10. Representative waveforms of total depolarization as a function of increasing hydrostatic pressure for the PSHZT ceramics.

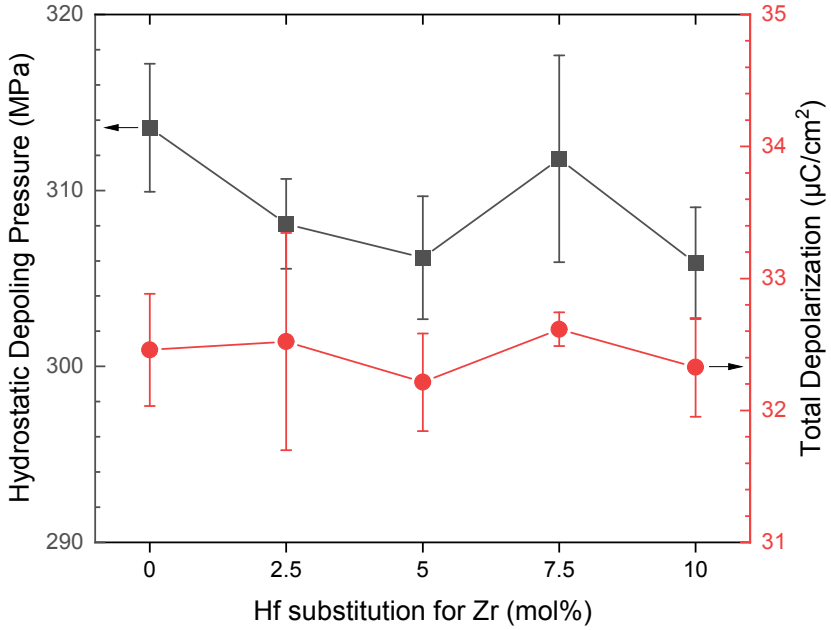

Figure 11. Hydrostatic depoling pressure and total depolarization as function of Hf substitution in the PSHZT ceramic.

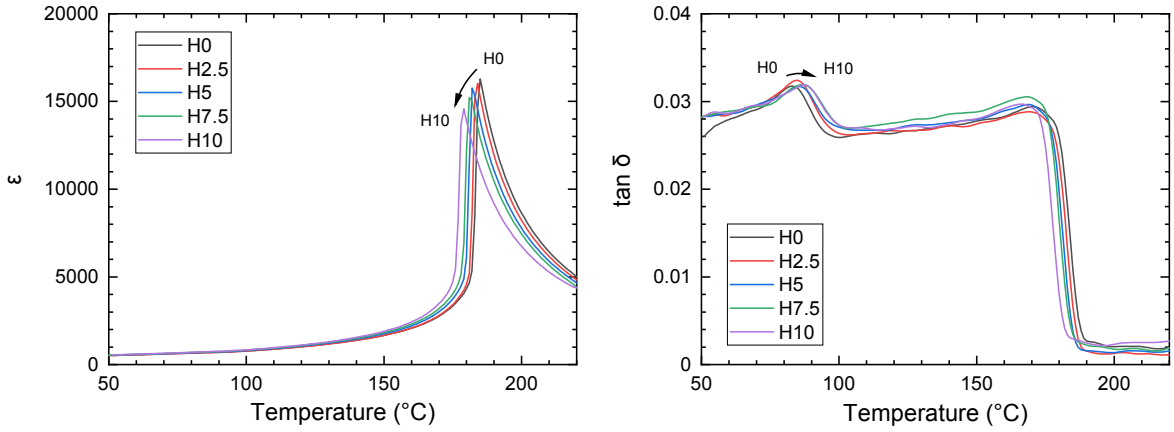

Figure 12. Permittivity and loss tangent as a function of temperature, upon cooling, for the PSHZT ceramics, measured at 1000 Hz.

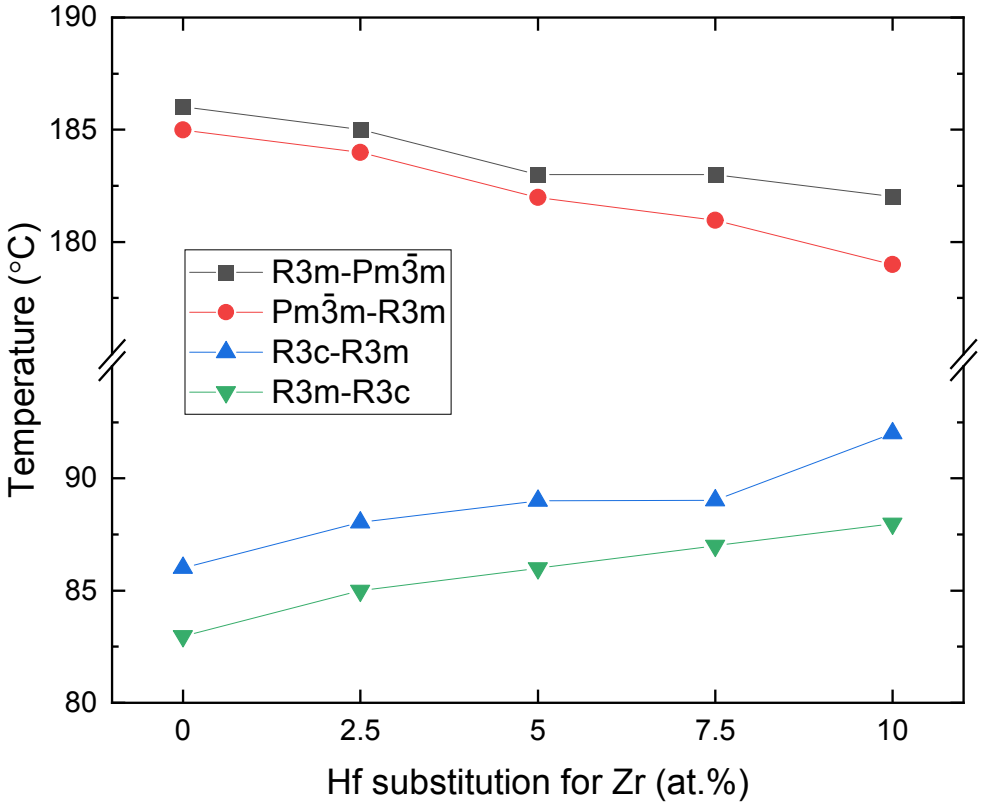

Figure 13. Phase transition temperatures as a function of Hf substitution in the PSHZT ceramics.